White Dwarf stars: Cosmic chronometers and dark matter probes

Maurizio Salaris[1] & Santi Cassisi[2]

[1]Astrophysics Research Institute, Liverpool John Moores University,
146 Brownlow Hill, Liverpool L3 5RF, UK
email: M.Salaris@ljmu.ac.uk

[2] INAF-Osservatorio Astronomico d'Abruzzo,
Via Mentore Maggini, I-64100 Teramo, Italy
email: cassisi@oa-teramo.inaf.it

January 29, 2018

Abstract

White dwarfs are the endpoint of the evolution of the large majority of stars formed in our galaxy. In the last two decades observations and theory have improved to a level that makes it possible to employ white dwarfs for determining ages of the stellar populations in the disk of the Milky Way and in the nearest star clusters, and constrain the existence and properties of dark matter candidates. This review is centred on white dwarf models, age-dating, and dark matter identification methods, recent results and future developments of the field.
Keywords: Dark matter, Galaxy:formation, Stars: interiors, white dwarfs

1 Introduction

White dwarf (WD) stars represent the final evolutionary stage of stars born with initial masses smaller than about 10 $M_{\odot}$. Given that for a standard initial mass function (IMF, the function that gives the relative number of stars born with different values of the mass M in a star formation episode) the large majority of stars are or will become WDs, together with the existence of a well defined relationship between their age (also denoted as cooling time) and luminosity, and their slow evolutionary speed, WDs have been considered as attractive candidates to unveil the star formation history of the Milky Way. During the last two decades, observations and theory have improved to a level that makes

possible to employ WDs for determining ages of the field stellar population in the solar neighbourhood, and in the nearest star clusters. WD cosmochronology is by now an additional independent method that complements other age-dating techniques based on main sequence turn-off stars (stars at the end of their main core H-burning phase, see e.g. the review by Vandenberg et al., 1996), gyrochronology (relations based on the evolution of the surface rotation rates of solar-like stars, see e.g. Barnes, 2007), nucleocosmochronometry (based on the use of surface abundances of radioactive nuclides like thorium and uranium, see e.g. Fowler & Hoyle, 1960).

Due to their high densities and relatively low temperatures, WDs have also been used as laboratories for astroparticle physics; in recent times this line of research has focused on testing the existence and properties of the axion, one of the best dark matter candidates.

This short review will summarize the main characteristics of WD evolution (Sect.2), the age-dating methods employing WDs (sect. 3), and how these stars are used to reveal the existence and constrain properties of dark matter particle candidates (Sect. 4). A short discussion about future developments will close the paper.

2 White Dwarf evolution in a nutshell

The large majority of WDs, i.e. those originated from progenitors with initial mass between ∼0.8-1.0 and $\sim 6-7 M_{\odot}$, have masses (M_{WD}) between ∼0.5 and $\sim 1.0\ M_{\odot}$ (see top panel of Fig. 1), and are made mainly (about 90% of the total mass) of an electron degenerate core of essentially carbon and oxygen, plus trace abundances of elements heavier than He (so-called 'metals'). WDs with masses ∼1.1-1.2 $M_{\odot}$ (originated from progenitors with initial mass between $\sim 6-7 M_{\odot}$ and $\sim 10\ M_{\odot}$) have an electron degenerate core of basically oxygen and neon composition. Stars born with mass below ∼0.8-1.0 $M_{\odot}$ (the precise value depending on the initial chemical composition) have not reached yet the WD phase, given that their pre-WD evolutionary times are longer than the age of the universe ($\sim$ 13.5 Gyr).

There is a large difference between the mass of a star at birth, and its final WD mass, caused by episodes of very efficient surface mass loss during the previous asymptotic giant branch (AGB) evolutionary phase. The strong AGB mass loss rates are the reason why –for single stars– even WDs formed from more massive progenitors do not reach the Chandrasekhar mass, that is the upper mass limit for the stability of electron degenerate stars. Some WDs originated from progenitors with initial mass below $\sim 2.0 M_{\odot}$, stripped of their envelope during the Red Giant Branch (RGB) phase (e.g. in interacting binary systems), have masses below $0.5 M_{\odot}$ and have a degenerate helium core.

In all cases, the WD electron degenerate core is surrounded by a non-degenerate layer of pure He with mass of the order of $M_{He} \sim 10^{-2}\ M_{WD}$ or less. This He-layer can be, in turn , surrounded by a H-layer with mass of the order of $M_H \sim 10^{-4}\ M_{WD}$ or less.

The WD radius follows a well defined mass-radius (M-R) relationship, with more massive objects having smaller radii (there is a small dependence of M-R relationship on the thickness of the surface H and He layers and the exact chemical stratification in the electron degenerate cores). Typical WD radii are of the order of 0.01 times the solar radius.

Due to the high surface gravities of WDs, the heavy elements in the envelope have settled at the bottom of the He-layer on very short timescales after the WD formation (Koester, 2009). WDs are spectroscopically denoted as DA if they have a pure-H outer envelope, or non-DA in case of no hydrogen in the outer layers. Among non-DA WDs, the DB subclass denotes objects with a pure He-envelope. Observationally the number ratio non-DA/DA changes with temperature for WDs in the solar neighborhood. For the range of luminosities of interest here, Tremblay & Bergeron (2008) find empirically an increase of the non-DA/DA ratio when the surface temperature (denoted as 'effective temperature') T_{eff} decreases below $\sim$ 10000 K, which is ascribed to convective mixing of thin H-envelopes with the more massive underlying He-layers. Other types of non-DA objects, which usually appear at low T_{eff}, arise most likely from convective mixing of the He-layer with underlying metals, and/or accretion of metals from the interstellar medium. This review will be focused on WDs with a carbon oxygen (CO) core –that constitute the large majority of WDs observed in stellar systems– and will consider DB models as templates for the evolution of non-DA WDs (see also Salaris, 2009, for a similar review of WD evolution.)

The basic structure of a WD is simple. The mass is contained mainly in the CO core, that is nearly isothermal because of the high electron conductivity. There are no active nuclear burnings (with the exception of possible residual H-burning in the envelope when the WD is hot and bright, and when the H-rich layers are massive enough) hence the WD evolution is a cooling process, whereby the core acts as the energy reservoir (the energy available to be radiated away is the internal energy of the non-degenerate CO ions), the outer non-degenerate layers determine the rate of energy outflow, and both surface luminosity and core temperature decrease with time.

The bottom panel of Fig. 1 displays the evolution in the Hertzsprung-Russell diagram (HRD, that displays the evolution of the surface bolometric luminosity L as a function of effective temperature T_{eff}) of WDs of different masses, and the previous evolution of three selected progenitors.

WDs start their evolution as bright and hot objects with surface luminosities of the order of 10^2-10^3 solar luminosities, and T_{eff} of the order of 10^5 K (higher mass WDs are born with higher L and T_{eff}). The main stages of WD cooling are sketched below (see also Salaris, 2009). The figures for the luminosity ranges (all expressed, as customary, in units of solar luminosity $L_{\odot}$) are indicative, for more precise values depend on the exact core chemical stratification, the WD core mass, and the chemical composition (and mass thickness) of the non-degenerate envelope.

$\log(L/L_{\odot}) > -1.5$. The brightest (hottest) stages of WD evolution are dominated by neutrino emission (mainly plasma-neutrinos, see e.g. Haft et al., 1994). If the total mass of the H-envelope is above a threshold of $\approx 10^{-4} M_{WD}$ (the

exact value depending on the WD mass), hydrogen burning through the *pp* chain becomes effective. Pulsational studies so far constrain the M_H to values generally below this threshold, see, e.g., Castanheira & Kepler (2008).

$-3 < \log(L/L_\odot) < -1.5$. The main source of energy is the internal energy of the ions. In the core the Coulomb parameter Γ (the ratio between Coulomb potential energy and thermal energy of the ions) is above unity, i.e. the ions are in the liquid phase and the ionic specific heat per unit mass increases compared to the gas phase. Another important process (and energy source) that is effective in the liquid phase is the diffusion of ^{22}Ne. This trace element is mainly produced during the previous core He-burning phase of the WD progenitor through the $^{14}N(\alpha,\gamma)^{18}F(\beta^+)^{18}O(\alpha,\gamma)^{22}Ne$) (where α denotes a ^4He nucleus). By virtue of its two excess neutrons (relative to the predominant A = 2Z nuclei), a downward force of $\approx 2m_pg$ (where m_p is the proton mass and g the local acceleration of gravity) is exerted on ^{22}Ne in the WD interior. This forces these nuclei to settle toward the centre of the WD; the sinking stops at the crystallization boundary, when the ions in the core start the transition to the solid phase. This change of Ne abundances causes a release of energy (see Eq. 1 below). Ne-diffusion provides an important energy contribution only for progenitors born in metal rich stellar populations (solar metallicity and above), because of a larger amount of neon in the CO core (typically about 2% mass fraction at solar metallicity).

$\log(L/L_\odot) < -3.0$. The Coulomb parameter Γ reaches the critical value $\Gamma_{cryst} \sim 180$, and the ions in the core undergo a phase transition from liquid to solid. The higher the WD mass, the earlier (at brighter luminosities and higher core temperatures) the onset of crystallization. This process introduces two new energy sources. The first one is the latent heat of crystallization, $\sim K_BT$ per crystallized ion, where K_B is the Boltzmann constant. The second source arises from the phase diagram of the CO binary mixture, see, e.g., Isern et al. (2000) and Fig. 2. In brief, the equilibrium compositions of a CO mixture in the solid and liquid phases are not the same, and the net effect is a migration of oxygen towards the central regions with the consequent release of gravitational energy (see Fig. 3 and Eq. 1).

Debye cooling. When crystallization of the CO core is essentially complete, the specific heat decreases according to the Debye law (it becomes proportional to T^3). The energy provided by the compression of the non-degenerate envelope (through the virial theorem) becomes now important.

As shown in Isern et al. (1997), for a WD made of two chemical species with mass fractions $X_h + X_l = 1$, where h denotes the heavier component, the local detailed energy budget of a WD at a given radial distance r from the centre is given by:

$$-(\frac{dL_{\rm r}}{dm}+\epsilon_\nu) = c_{\rm v}\frac{dT}{dt}+T\Big(\frac{\partial P}{\partial T}\Big)_{V,X_0}\frac{dV}{dt}-l_{\rm s}\frac{dM_{\rm s}}{dt}\delta(m-M_{\rm s})+\Big(\frac{\partial E}{\partial X_h}\Big)_{T,V}\frac{dX_h}{dt} \quad (1)$$

where E is the internal energy per unit mass, L the local luminosity, ϵ_ν the neutrino energy loss rate per unit mass, $V = 1/\rho$ is the specific volume,

c_V the specific heat at constant volume per unit mass, P the pressure, T the temperature, t the time and m the mass enclosed within radius r. The first term in the right-hand side arises from the heat capacity of the star, the second one from the energy contribution due to changes in volume, which is usually negligible (the radius does not stay exactly constant, but changes very slowly with time), apart from the last stages of cooling. The third term stems from the energy contribution due to the latent heat release upon crystallization ($l_{\rm s}$ is the latent heat of crystallization and dM_s/dt is the rate of growth of the solid core due to crystallization). The delta function specifies that the latent heat is released at the solidification front. The last term arises from the energy released by the change of chemical abundances in the core –chemical separation or diffusion. Figure 3 displays the effect of chemical separation upon crystallization on a $0.61 M_{\odot}$ model, with H layers of mass $M_H = 10^{-4} M_{WD}$ and He layers $M_{He} = 10^{-2} M_{WD}$. The delay in the cooling process caused by this phenomenon is comparable to the effect of latent heat release.

The detailed WD energy budget depends on the chemical stratification of the core and envelope. Variations of the chemical composition of the core affect the internal energy available to be radiated away (through the variation of the number of ions), the latent heat release and the chemical redistribution upon crystallization, as discussed also in Salaris (2009). Variations of the composition and mass of the non-degenerate envelope affect the rate of energy release because of the change of opacity. In general, envelopes with thinner or absent H-layers speed up the cooling process.

Predictions from stellar evolution calculations are currently subject to uncertainties regarding the CO profiles and envelope stratification at the onset of WD cooling. As for the CO profile, the main culprit is not only the uncertainty in the $^{12}C + \alpha$ reaction rate –estimated to be of the order $1\sigma = \pm 30$ % according to Kunz et al. (2002)– that determines the final C/O ratio at the end of the previous core He-burning phase but also –and even more importantly– the uncertain treatment of core convection during the same burning stage. As discussed in detail by Straniero et al. (2003), for a given stellar mass, various possible treatments of core mixing can alter substantially the final CO profile.

Regarding the envelopes, uncertainties in the mass-loss efficiency during the AGB phase do not allow firm predictions of their chemical composition and thickness at the start of WD cooling. The uncertainty in the mass-loss efficiency along the AGB affects also the CO stratification in a more subtle way. In fact, changing the mass-loss efficiency affects the initial-final WD mass relationship (IFMR) and the relationship between the mass of the CO core (and associated chemical profile) at the end of central He-burning, and at the end of the AGB phase.

Figure 4 shows numerical tests (Salaris, 2009) that give an order-of-magnitude estimate of uncertainties on cooling times due to different CO profiles. The cooling times of a $0.61 M_{\odot}$ WD (this is a typical mass for WDs in the solar neighbourhood, close to the value of the mode of the mass distribution determined recently by Limoges et al., 2015) with $M_H = 10^{-4} M_{WD}$ and $M_{He} = 10^{-2} M_{WD}$ are computed assuming 4 different core chemical profiles. The solid line repre-

sents the reference profile of Fig. 3, the dashed-dotted line shows a flat CO profile with equal abundances (an unrealistic profile to maximize the effect of chemical separation), the dashed line represents the effect of an alternative treatment of He-burning core convection, following Straniero et al. (2003) results, the dotted line accounts for a different IFMR (progenitor with a smaller initial mass). The largest effect compared to the reference model is obtained with the flat CO stratification, that causes an age increase of the order of 10−15% for the oldest WDs. The other profiles shown in the figure cause a reduction of cooling times by less than 10%. The age uncertainty becomes negligible before the models start crystallization.

Figure 5 shows how cooling times (time since WD formation as a function of the surface luminosity) depend on the assumed envelope composition. The H-atmosphere models are calculated with $M_H = 10^{-4} M_{WD}$ and $M_{He} = 10^{-2} M_{WD}$, whilst the He-atmosphere models have $M_{He} = 10^{-3.5} M_{WD}$ (Salaris et al., 2010). The He-atmosphere WD evolution is much faster, because in this regime the opacity is lower in He layers. As a general rule, decreasing the thickness of the H-layers increases the cooling speed of the models.

Figure 6 gives insights into the evolution of the inner structure of typical WDs, with H- and He-atmospheres. We display the mass location of the H-He and He-CO interface, the crystallization front, the lower boundary of surface convection and the location of the local Fermi temperature T_F, as a function of the surface luminosity (the lowest luminosity in the diagrams correspond approximately to the brightness of the faintest WDs observed in our galaxy). The electron degeneracy advances slowly towards more external layers with decreasing luminosity, whilst surface convection gets deeper and eventually overlaps with the degenerate layers of the H or He envelopes (this phenomenon is called 'convective coupling' Fontaine et al., 2001). Notice that less massive WDs display deeper (in mass) convective regions. It is obvious then how thin (in terms of mass) H- and He-layers would induce mixing between the convective envelope and the external layers of the CO core.

3 White Dwarf cosmochronology

The working tools for WD age-dating are WD isochrones, i.e. the HRDs of WDs originated from progenitors born in a single *instantaneous* star formation episode (see, Fig. 7). These so-called single-burst, single-metallicity populations are created in what corresponds to an elementary star formation episode, that gives origin to coeval stars covering a range of masses and with the same initial chemical composition. The mass distribution of the formed stars follows a given IMF. Populations hosted in star clusters are well approximated by single-burst, single-metallicity populations, whilst the field population of, for example, the disk of the Milky Way is created by a continuous sequence of elementary star formation episodes.

Figure 7 displays cooling tracks (H-atmospheres) for different WD masses (hence progenitor masses) in the HRD, and a few WD isochrones of different

ages. Essentially, for each WD track one calculates the total age t_{WD} from the formation of the progenitor (progenitor lifetime until WD formation + WD cooling age) and, for a given population age t, the resulting isochrone is the line that joins the points (one per cooling track) where the t_{WD}=t. Different points along an isochrone are populated by WDs with different mass (formed from progenitors of different intial mass). Notice that more massive WDs are located at the bottom of the isochrone (hence the turn towards higher T_{eff} that correspond to lower radii) because they are originated from more massive and shorter lived progenitors, hence they had more time to cool for a given t. It is also clear that increasing t decreases the luminosity of the bottom end of the isochrones, because of the longer WD cooling times. The bottom end of the observed WD sequence is therefore the age indicator for the parent population.

Comparisons with observations require the isochrones to be transposed to an observational colour-magnitude-diagram (CMD), whereby observations in photometric filters provide magnitudes and colours (differences of magnitudes between a pair of filters), that are the observational counterparts of L and T_{eff}. Isochrones in the HRD are transposed to a CMD using bolometric corrections calculated from WD model atmospheres (see, e.g., Bergeron et al., 1995), as shown in Fig. 7.

From a WD isochrone, the differential luminosity function (LF - star counts as a function of magnitude) in a given passband can be calculated after assuming an IMF for the WD progenitors. It is usually the LF that is employed for WD age-dating of star clusters and field population, and in this case the age indicator is the cut-off luminosity beyond which the star counts drop to zero. Figure 8 displays an example of age dating with the WD LF in case of the globular cluster M 4 (Bedin et al., 2009). The left-hand panel displays the observed WD cooling sequence (in a pair of photometric filters of the ACS camera on board the *Hubble Space Telescope*), whilst the right-hand panel shows the corresponding observed LF and theoretical counterparts for various ages, corrected for the distance and extinction towards the cluster line of sight (absorption due to interstellar gas and dust). Ages too high or too low do not match the magnitude of the peak and cut-off of the observed LF. Typically, the F606W magnitude of the LF cut-off changes with age by $\sim$0.2 mag/Gyr at old ages (order of 10 Gyr), and $\sim$0.5 mag/Gyr at intermediate ages (order of 1-2 Gyr).

Even with the *Hubble Space Telescope* we have been able to detect the bottom of the WD sequence only in three of the nearest globular clusters (NGC6397, M 4, 47 Tuc, see Hansen et al., 2004, 2007, 2013; Bedin et al., 2009; Richer et al., 2013), while a much larger sample of open clusters has been age-dated with WDs (von Hippel, 2005; Bedin et al., 2008; Bellini et al., 2010; Bedin et al., 2010; García-Berro et al., 2010).

Regarding field WDs, Fig. 9 displays the most recent determination of the LF for WDs in the disk of our galaxy. The shape of this LF is quite different from the case of star clusters, because of the extended star formation history of the parent population. However, there is still a well defined cut-off due to the finite age of the galaxy. It is usually assumed a constant star formation

rate between now and the maximum age of the galactic disk[1], that is estimated by matching the luminosity of the LF cut-off. The most recent estimate is by Kilic et al. (2017), who derived maximum ages ∼8 Gyr for the thin disk, and ∼9 Gyr for the thick disk of the Milky Way, respectively. However the models employed for this estimate do not include the effect of phase separation upon crystallization and neon diffusion, therefore the age is underestimated.

Even if the star formation rate has not been precisely constant in the past, the estimate of the age of the oldest disk WDs is essentially unaffected (see, e.g., Torres & García-Berro, 2016) In case of halo field WDs, due to their larger distances the LF cut-off luminosity has not been detected yet.

Figure 10 summarizes the status of the Milky Way formation chronology based on WDs, showing ages estimated for the three globular clusters listed above, the thin and thick disk components of the Milky Way, and the age of the oldest open cluster belonging to the thick disk of our galaxy.

4 White dwarfs as dark matter probes

Astronomical observations continue to provide overwhelming evidence for a dark component of matter in the Universe. The presence of dark matter (DM) is not only supported by the observed flat rotation curves of galaxies, but also by gravitational lensing that clearly indicates that the masses of galaxies acting as lenses for foreground sources (quasars) are greater than can be accounted for by their luminous component (see, e.g Del Popolo, A., 2014, for a review). The nature of the DM is however still a major unsolved problem.

Several DM candidates have been put forward, amongst them weakly interacting massive particles (WIMPs) are attractive ones. These are stable massive particles, neutral and weakly interacting with ordinary matter, and currently are supposed to be of supersymmetric nature. As discussed in, i.e., Bertone & Fairbairn (2008) and Amaro-Seoane et al. (2016), stars in regions of high DM densities (for example close to the centre of our galaxy) may experience the accretion of a large amount of DM. The capture of DM onto stars is proportional to the product of the number of nucleons in the star with the escape velocity, and therefore compact objects such as WDs are ideal targets for searches aimed at detecting the effects of DM accretion. Supersymmetric WIMP particles are assumed to be Majorana particles (a Majorana particle is a fermion that is its own antiparticle) hence, once captured, they can annihilate themselves at a certain annihilation rate. This would produce extra energy that will make WDs anomalously bright compared to standard WD models At the moment there are no observational hints that this is indeed happening.

There exists at least another class of DM candidates (axions), whose existence can be tested employing WDs. Axions are weakly interacting hypothetical particles, proposed several decades ago to solve the so-called strong CP prob-

[1]An algorithm that inverts the WD LF to obtain a maximum likelihood estimate of the time-varying star formation rate of the host stellar population has been recently developed by Rowell (2013)

lem (where CP stands for *charge+parity*) in quantum chromodynamics (see, e.g., Peccei & Quinn, 1977). Besides their relevance for the standard model of particle physics, axions are natural candidates to explain the non-baryonic dark matter content of the universe. Their contribution to DM depends on their mass, which determines the intensity of the coupling with matter, and it is not constrained by the theories that predict the existence of these particles (Raffelt, 2007).

There are two categories of axion models: the KVSZ model (Kim, 1979; Shifman et al., 1980), where the axions couple with photons and hadrons, and the DFSZ model (Dine et al., 1981), where they also couple to charged leptons like electrons. WD theoretical models have focused on DFSZ axions. The coupling strength to electrons is defined through a dimensionless coupling constant, $g_{\rm ae}$, related to the mass of the axion, $m_{\rm a}$, through the relation:

$$g_{\rm ae} = 2.8 \times 10^{-14}\ \frac{m_{\rm a} \cos^2 \beta}{1\ {\rm meV}}, \tag{2}$$

where $\cos^2 \beta$ is a free, model-dependent parameter, usually set equal to unity.

At the typical temperatures and densities of WD cores, the emission of DFSZ axions is expected to take place mainly through bremsstrahlung (Raffelt, 1986). The axion emission rate is given by (Nakagawa et al., 1987, 1988):

$$\epsilon_{\rm a} = 1.08 \times 10^{23} \frac{g_{\rm ae}^2}{4\pi} \frac{Z^2}{A} T_7^4 F(T,\rho)\ \ [{\rm erg\ g^{-1}\ s^{-1}}] \tag{3}$$

where T_7 is the temperature in units of 10^7 K, and the function $F(T,\rho)$ takes into account the Coulomb plasma effects. Since axions interact very weakly with the stellar matter, their production would increase the cooling rate compared to models without axion production, with more massive axions producing larger additional cooling. Figure 11 displays the effect of axions on the luminosity and cooling timescales of a typical $0.61 M_{\odot}$ WD model. The left-hand panel displays the surface photon luminosity, plus neutrino and axion luminosities (energy loss per unit time) with increasing $m_{\rm a} \cos^2 \beta$, as a function of the bolometric magnitude ${\rm M_{bol}} = -2.5 {\rm log}(L/L_{\odot}) + 4.75$ (L is the surface photon luminosity). For increasing $m_{\rm a} \cos^2 \beta$ the axion luminosity increases, and the neutrino luminosity very slightly decreases. The right-hand panel of the same figure displays the fractional difference in cooling times between the calculations without axions and models including these particles. The largest differences appear at M_{bol} ∼9-10, corresponding to $\log(L/L_{\odot}) \sim -2$.

It is important to emphasize that investigations about axion properties based on WDs must assume that all other mechanisms of energy production and energy loss in WDs are properly modelled, and any discrepancy between observed and theoretical cooling speed is due to axions.

Isern et al. (2008) and Isern et al. (2009) included axion emissivity in WD evolutionary models and found an improved agreement between the theoretical calculations of the bright part of the LF of field disk WDs and observations. This provided the first indication for the existence of axions.

More accurate inferences have come recently from the study of pulsating WDs. Pulsating WDs are characterized by multiperiodic brightness variations caused by non-radial modes (g-modes), caused by gravity waves excited by the so-called κ-mechanism (essentially due to variations of the opacity in the partial ionization regions near the surface during compression and expansion, see e.g. Winget & Kepler, 2008, and references therein). The spatial configuration of the oscillation modes is defined by the radial order n (n=0, 1,2...) which is the number of nodes in the radial direction, the harmonic degree l (l=0,1,2...) and the azimuthal order m ($m = -l, -l+1.... + l$), which determine the behaviour of the mode over the stellar surface. The observed pulsating WDs display g-modes with $\ell \leq 2$, and periods between 70 and 1500 s (Winget & Kepler, 2008). The star G117−B15A (a DA WD) is the best studied member of this class of variables, and displays oscillation periods Π of 215.20 s (l=1, n=2) , 270.46 s (l=1, n=3) and 304.05 s (l=1, n=4). The rate of change of the 215 s mode with time has been measured to be $\dot{\Pi} = (4.19 \pm 0.73) \times 10^{-15}$ s/s (Kepler, 2011). In addition, there are constraints on mass, surface gravity and T_{eff} coming from spectroscopy.

The rates of period change of pulsation g-modes yield information about the WD cooling speed: As the WD evolves the core temperature decreases, and the pulsational spectrum shifts to longer periods.

The recent theoretical analysis by Córsico et al. (2012) has determined the mass (0.593±0.007 $M_{\odot}$), luminosity ($\log(L/L_{\odot})$=−2.50±0.03) H- and He-envelope masses, and central C/O ratio by matching theoretical WD models to the observed spectroscopic and pulsational constraints. The ability to determine envelope mass and composition, and central C/O ratio greatly reduce the theoretical uncertainties on the cooling speed of the appropriate WD cooling model.

Córsico et al. (2012) found a theoretical $\dot{\Pi}^{\rm t} = (1.25 \pm 0.09) \times 10^{-15}$ s/s, more than 3 times lower than observed, if no axion production is included in the calculations. This means that the model cools down more slowly than the observed WD. The mass of the axion necessary to match the observed rate of period change (maintaining consistency with the observed periods) is $m_{\rm a} \cos^2 \beta = \left(17.4^{+2.3}_{-2.7}\right)$ meV, where the errors come mainly from errors in the measurement of $\dot{\Pi}$.

Even more recently, a similar analysis performed on the pulsating DB WD PG 1351+489 (Battich et al., 2016) has provided an upper mass limit $m_{\rm a} \cos^2 \beta \leq$ 11.5 meV.

5 Discussion

Observations of WDs and their interpretation by means of theoretical WD evolutionary models are providing important information about the past evolution of our galaxy and the nature of DM. A crucial requirement for this kind of analyses is the accuracy of the physics inputs included in the theoretical calculations (e.g., equation of state, CO phase diagram, neutrino energy losses,

surface boundary conditions). It is still difficult to assess how accurate these physics inputs really are, like for example the equation of state of cold WDs, . There have been a few theoretical studies to assess the sensitivity of the predicted cooling times to uncertainties in the model core and envelope chemical stratification and electron conduction opacities (e.g. Hansen, 1999; Prada Moroni & Straniero, 2007; Salaris, 2009; Salaris et al., 2010) and photospheric boundary conditions (e.g. Hansen, 1999; Salaris et al., 2000; Rohrmann et al., 2012); however there is no modern systematic study of the effect of employing different equations of state (but see below) and radiative opacities, especially the less established low-temperature opacities in cool WD models. Very recently Salaris et al. (2013) have assessed for the first time the maximum possible accuracy in the current estimates of WD cooling times, resulting only from the different implementations of the stellar evolution equations and homogeneous input physics in two independent stellar evolution codes. This accuracy amounts to $\sim$2% at luminosities below $\log(L/L_{\odot})\sim -1.5$. This difference is smaller than the uncertainties in the input physics and chemical stratification explored so far. The work by Salaris et al. (2013) has also explored for the first time (but not exhaustively) the role played by different equation of states adopted in the model calculations, that can induce differences in the cooling times by $\sim$20-30% for crystallizing WD models.

From an observational point of view, the GAIA satellite (Evans et al., 2017) will find 250000 to 500000 field WDs, opening a new era in the study of the Milky Way field disk and halo WD LF. However, it won't detect the cut-off of the field halo LF. Also, a large increase of the globular cluster sample size with detected LF cut off is expected with the soon to be launched James Webb Space Telescope. The sample will be increased from three to eleven clusters, and the intercomparison between WD ages and ages from main-sequence turn-off stars will provide a more stringent assessment of the accuracy of WD models.

Regarding pulsating WDs and axions, three additional objects, namely R548 (a DA WD), KIC8626021 and EC20058-5234 (both DB WDs) are promising candidates for evaluating $m_{\rm a}\cos^2\beta$. This will enable us to check the consistency of the results on a larger sample of pulsating WDs, and put stronger constraints on the existence and properties of these elusive particles.

References

Amaro-Seoane, P., Casanellas, J., Schödel, R., Davidson, E., & Cuadra, J. 2016, *MNRAS*, 459, 695

Barnes, S. A. 2007, *ApJ*, 669, 1167

Battich, T., Córsico A. H., Althaus, L. G., & Miller Bertolami, M. M. 2016, *JCAP*, 08, 062

Bellini, A. et al. 2010, *A&A*, 513, 50

Bedin, L. R., King, I. R., Anderson, J., Piotto, G., Salaris, M., Cassisi, S., & Serenelli, A. 2008, *ApJ*, 678, 1279

Bedin, L. R., Salaris, M., Piotto, G., Anderson, J., King, I. R., & Cassisi, S. 2009, *ApJ*, 697, 965

Bedin, L. R., Salaris, M., King, I. R., Piotto, G., Anderson, J., & Cassisi, S. 2010, *ApJ*, 708, L32

Bergeron, P., Wesemael, F., & Beauchamp, A. 1995, *PASP*, 107, 1047

Bertone, G., & Fairbairn, M. 2008, *Phys. Rev. D*, 77.043515

Castanheira, B. G., & Kepler, S. O. 2008, *MNRAS*, 385, 430

Córsico, A. H., Althaus, L. G., Miller Bertolami, M. M., Romero, A. D., García-Berro, E., Isern, J., & Kepler, S. O. 2012, *MNRAS*, 424, 2792

Del Popolo, A. 2014, *International Journal of Modern Physics D*, 23, 1430005

Dine, M., Fischler, W., & Srednicki, M. 1981, *Phys. Lett. B*, 104, 199

Evans, D. W. et al. 2017, *A&A*, 600, 51

Fontaine, G., Brassard, P., & Bergeron, P. 2001, *PASP*, 113, 409

Fowler, W. A. & Hoyle, F. 1960, *AnPhy*, 10, 280

García-Berro, E., Torres, S., Althaus, L. G., Renedo, I., Lorén-Aguilar, P., Córsico, A. H., Rohrmann, R. D., Salaris, M., & Isern, J. 2010, *Nature*, 465, 194

Haft, M., Raffelt, G., & Weiss, A. 1994, *ApJ*, 425, 222

Hansen, B. M. S. 1999, *ApJ*, 520, 680

Hansen, B. M. S. et al. 2004, *ApJ*, 155, 551

Hansen, B. M. S. et al. 2007, *ApJ*, 671, 380

Hansen, B. M. S. et al. 2013, *Nature*, 500, 51

Isern, J., Mochkovitch, R., García-Berro, E., & Hernanz, M. 1997, *ApJ*, 485, 308

Isern, J., García-Berro, E., Hernanz, M., & Chabrier, G. 2000, *ApJ*, 528, 397

Isern, J., García-Berro, E., Torres, S., & Catalán, S. 2008, *ApJ* , 682, L109

Isern, J., Catalán, S., & García-Berro, E. 2009, *J. Phys: Conf. Ser.*, 172, 012005

Kepler, S. O. 2011, in *ASP Conf. Ser. Proceedings of the 61st Fujihara Seminar: Progress in Solar/stellar Physics with Helio- and Asteroseismology*, Blackwell Science Ltd

Kim, J. E. 1979, *Phys. Rev. Lett*, 43, 103

Koester, D. 2009, *A&A*, 498, 517

Kilic, M., Munn, J. A., Harris, H. C., von Hippel, T., Liebert, J. W., Williams, K. A., Jeffery, E. & DeGennaro, S. 2017, *ApJ*, 837, 162

Kunz, R., et al. 2002, *ApJ*, 567, 643

Limoges, M.-M., Bergeron, P. & Lépine, S. 2015, *ApJS*, 219, 19

Munn, J. A. et al. 2017, *ApJ*, 153, 10

Nakagawa, M., Kohyama, Y., & Itoh, N. 1987, *ApJ* , 322, 291

Nakagawa, M., Adachi, T., Kohyama, Y., & Itoh, N. 1988, *ApJ* , 326, 241

Peccei R. D., & Quinn H. R. 1977, *Phys. Rev. Lett.* , 38, 1440

Pietrinferni, A., Cassisi, S., Salaris, M. & Castelli, F 2004, *ApJ*, 612, 168

Prada Moroni, P. G. & Straniero, O. 2007, *A&A*, 466, 1043

Raffelt G. G. 1986, *Phys. Lett. B*, 166, 402

Raffelt, G. G. 2007, *Journal of Physics A Mathematical General*, 40, 6607

Richer, H. B., et al. 2013, *ApJ*, 778, 104

Rohrmann, R. D., Althaus, L. G., García-Berro, E., Córsico, A. H., & Miller Bertolami, M. M. 2012, *A&A*, 546, A11

Rowell, N. 2013, *MNRAS*, 434, 1549

Shifman, M. A., Vainshtein, A. I., & Zakharov, V. I. 1980, *Nucl. Phys. B*, 166, 493

Salaris, M 2009, in *'The Ages of Stars', Proceedings of the International Astronomical Union, Cambridge University Press*, 258, 287

Salaris, M., Dominguez, I., García-Berro, E., Hernanz, M., Isern, J., & Mochkovitch, R. 1997, *ApJ*, 486, 413

Salaris, M., García-Berro, E., Hernanz, M., Isern, J., & Saumon, D. 2000, *ApJ*, 544, 1036

Salaris, M., Cassisi, S., Pietrinferni, A., Kowalski, P. M., & Isern, J. 2010, *ApJ*, 716, 1241

Salaris, M., Althaus, L. G., & García-Berro, E. 2013, *A&A*, 555, A96

Segretain, L., & Chabrier, G. 1993, *A&A*, 271, L13

Straniero, O., Dominguez, I., Imbriani, G., & Piersanti, L. 2003, *ApJ*, 583, 878

Torres, S., & García-Berro, E. 2016, *A&A*, 588, A35

Tremblay, P.-E., & Bergeron, P 2008, *ApJ*, 672, 1144

Vandenberg, D. A., Bolte, M. & Stetson, P. B. 1996, *ARA&A*, 34, 461

von Hippel, T. 2005, *ApJ*, 622, 565

Winget, D. E., & Kepler, S. O. 2008, *ARAA*, 46, 157

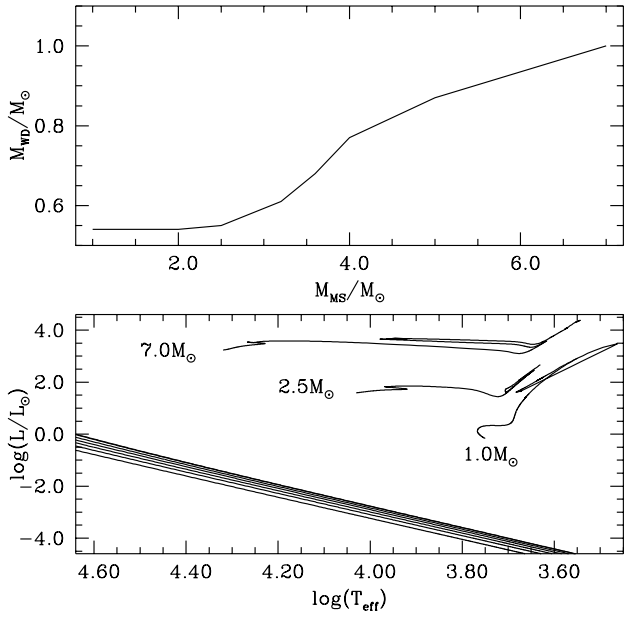

Figure 1: The top panel displays an approximate relationship between CO WD mass, and the progenitor initial main sequence mass denoted as M_{MS} (all in solar mass units) from the models by Pietrinferni et al. (2004). The bottom panel displays the evolution in the HRD of WDs with masses equal to 0.54, 0.55, 0.61, 0.68, 0.77, 0.87, and $1.0 M_\odot$ (Salaris et al., 2010), compared to previous evolutionary phases of three selected progenitors with the labelled initial masses.

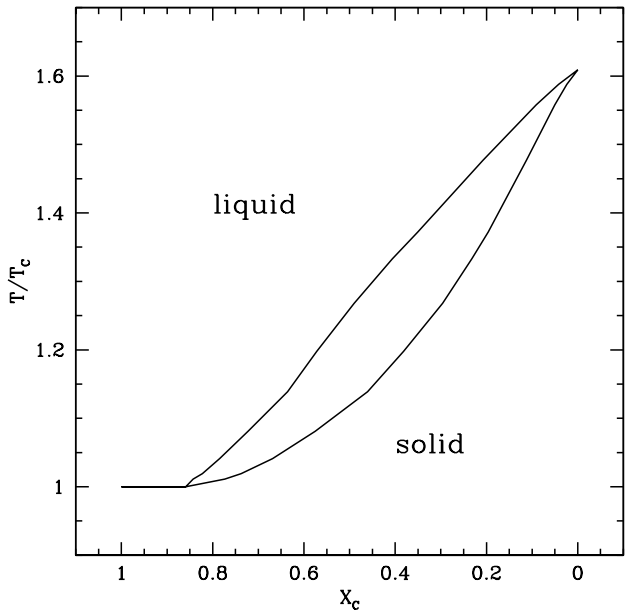

Figure 2: Phase diagram (Segretain & Chabrier, 1993) for a CO binary mixture. T_C denotes the crystallization temperature of a pure carbon mixture, and X_C is the carbon mass fraction.

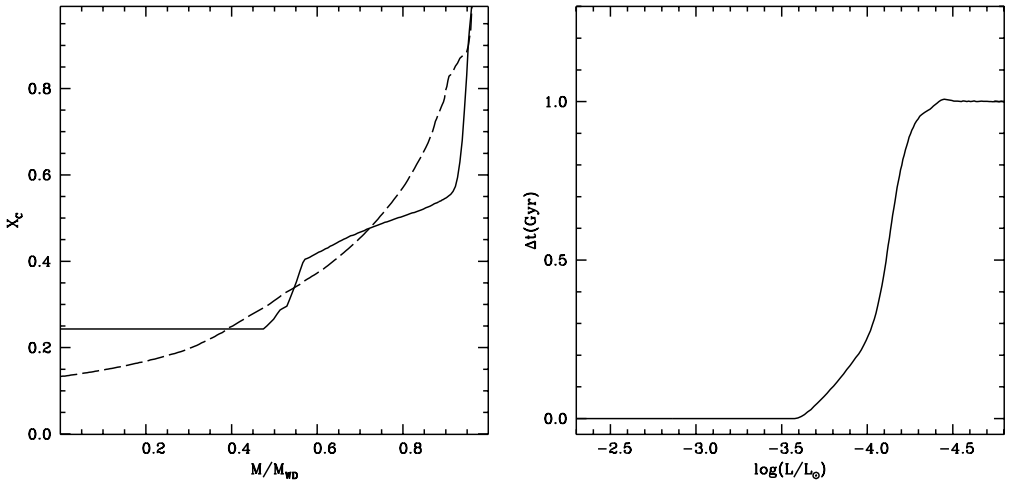

Figure 3: *Left* : Initial carbon abundance profile (in mass fraction; the corresponding oxygen mass fraction is $X_O = 1 - X_C$) in the core of a 0.61 $M_\odot$ WD model from Salaris et al. (1997) calculations (solid line), and after chemical redistribution upon crystallization (dashed line). *Right* : Time delay due to the chemical redistribution, from the models by Salaris et al. (2000).

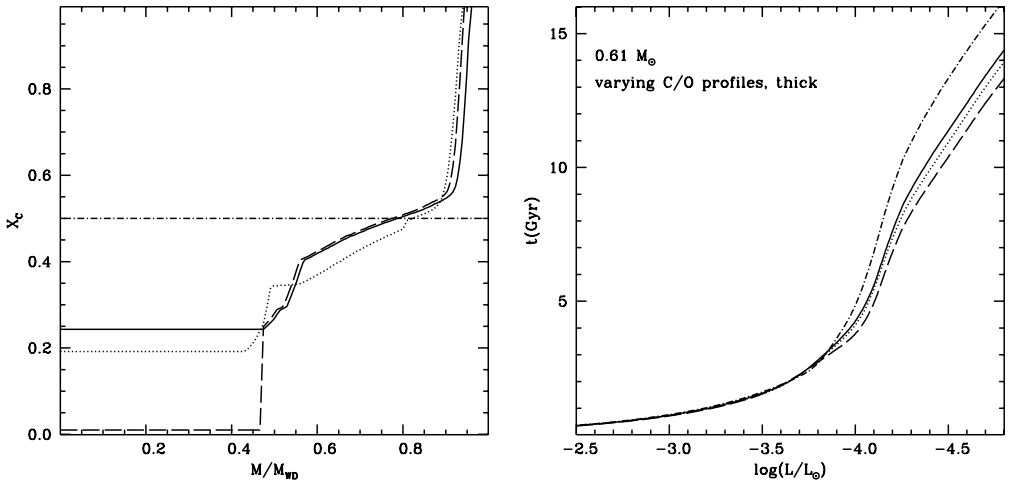

Figure 4: *Left* : Test carbon profiles in the core of a $0.61 M_\odot$ model (the oxygen mass fraction is essentially $X_O = 1 - X_C$). *Right* : Corresponding cooling timescales. From Salaris (2009) calculations (see text for details).

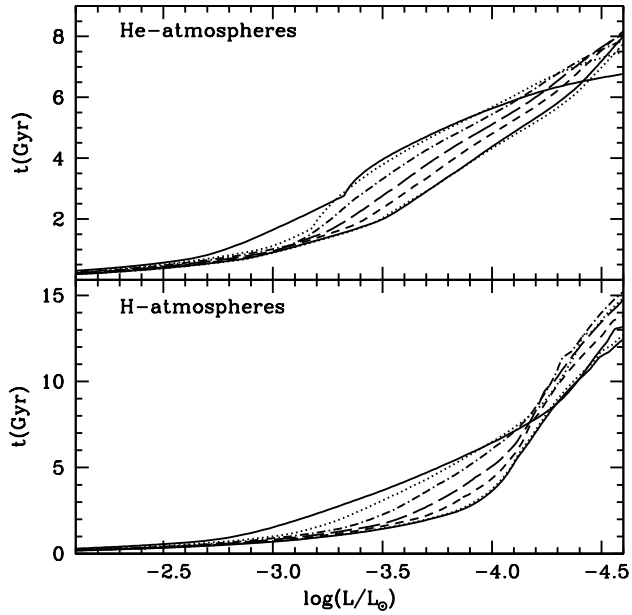

Figure 5: Cooling times as a function of the luminosity (in solar units) for WD models with the masses listed in Fig. 1 and either H (bottom panel) or He (top panel) atmospheres (models by Salaris et al., 2010). At a reference $\log(L/L_{\odot}) = -3.5$, WDs have with increasing mass have increasingly longer cooling times.

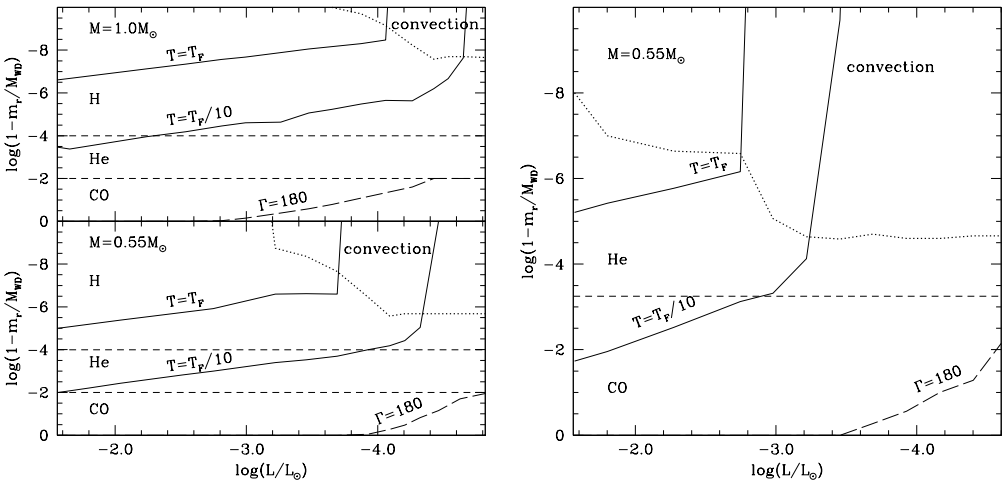

Figure 6: Evolution with luminosity of the inner mass boundary of surface convection (dotted lines). The H-He and He-CO chemical transitions are displayed as short dashed lines, and the composition of the various regions is labelled. The evolution with luminosity of the crystallization front is displayed with long dashed lines (labelled as $\Gamma = 180$), and the evolution of the mass location of the layers with temperature equal to the Fermi temperature, and 1/10 of the Fermi temperature, is shown with solid lines. The left panel displays two H-atmosphere models with the labelled masses, whilst the right panel displays one He-atmosphere model, all from the calculations by Salaris et al. (2010).

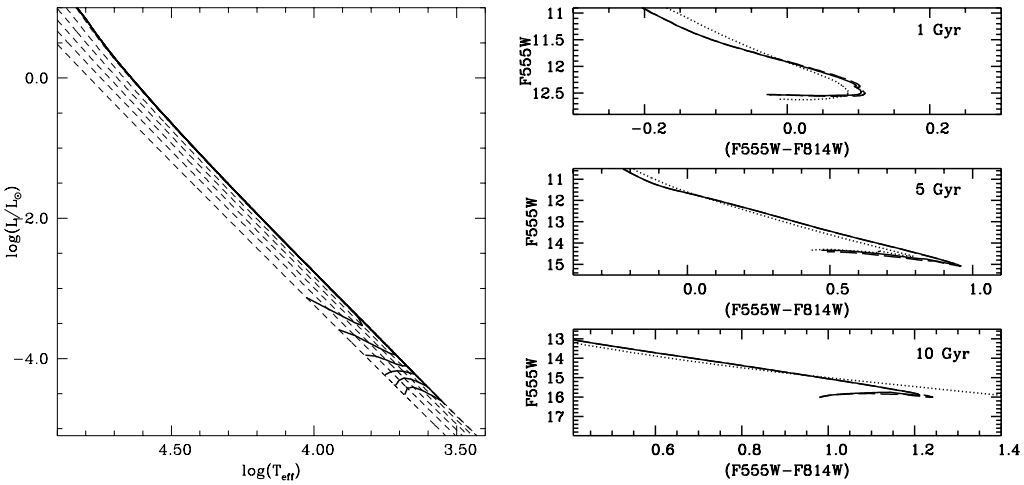

Figure 7: *Left* : HRD of a set of H-atmosphere WD tracks (dashed lines – the same as in Fig. 1), and WD isochrones (heavy solid lines) for ages equal to 2, 4, 6, 8, 10, and 12 Gyr (older isochrones display a fainter turn to hotter effective temperatures). *Right* : Isochrones for H-atmosphere (solid lines) and He-atmosphere (dotted lines) WDs with the labelled ages, displayed in a CMD employing a combination of filters of the ACS camera on board the *Hubble Space Telescope*.

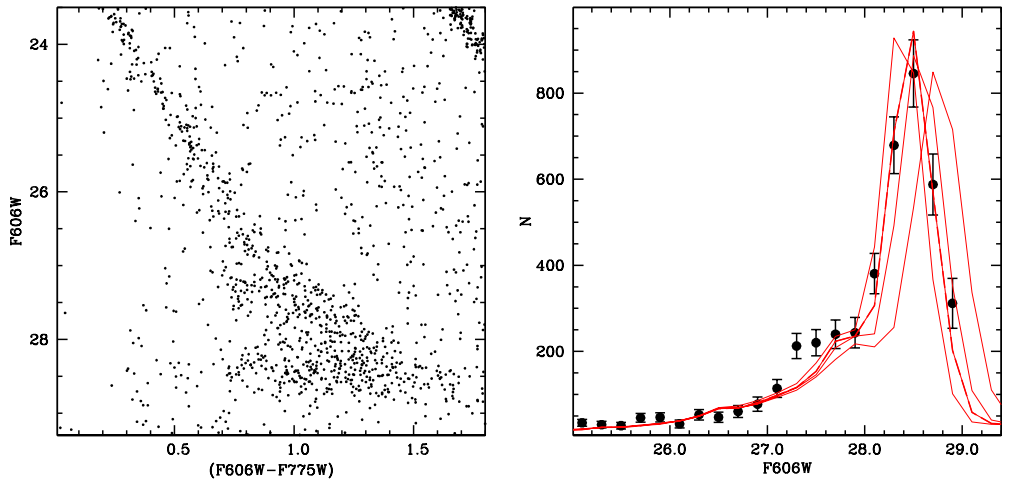

Figure 8: *Left* : Observed CMD of the WD cooling sequence in the globular cluster M4 (Bedin et al., 2009).*Right* : Observed LF (number N of stars per magnitude bin –filled circles with error bars) compared to theoretical ones for ages equal to 11, 11.6 (heavy solid line), 12 and 13 Gyr.

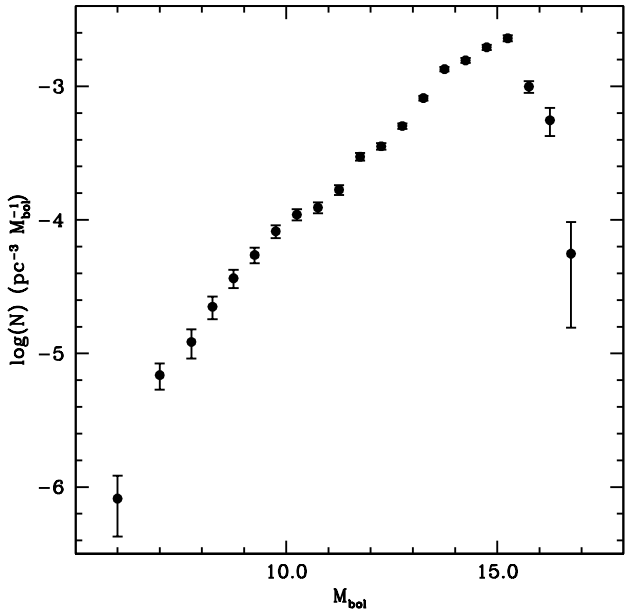

Figure 9: Observed LF (number of stars per unit of bolometric magnitude and cubic parsec) of WDs in the disk of the Milky Way (Munn et al., 2017), in bolometric magnitude bins ($M_{bol} = -2.5 \log(L/L_{\odot})+4.75$).

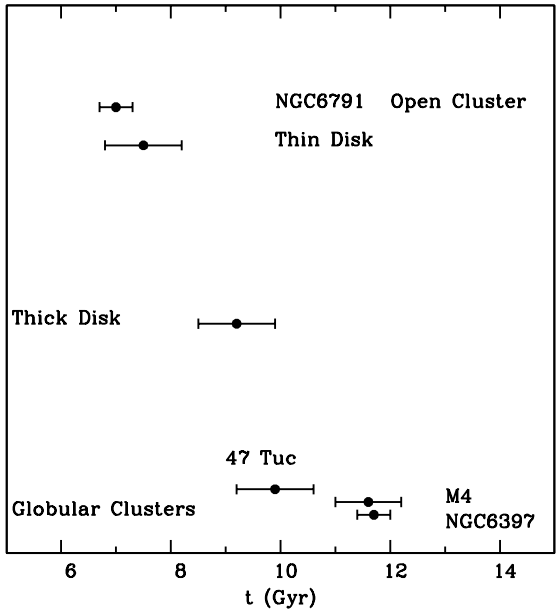

Figure 10: Estimated ages for a sample of globular clusters, field WDs and the oldest known open cluster, based on WD cosmochronology. From top to bottom the various systems are distributed in order of decreasing metallicity. Ages come from Bedin et al. (2008) for NGC 6791, Kilic et al. (2017) for thin and thick disk, Hansen et al. (2013) for 47 Tuc, Bedin et al. (2009) for M 4 and Hansen et al. (2007) for NGC 6397

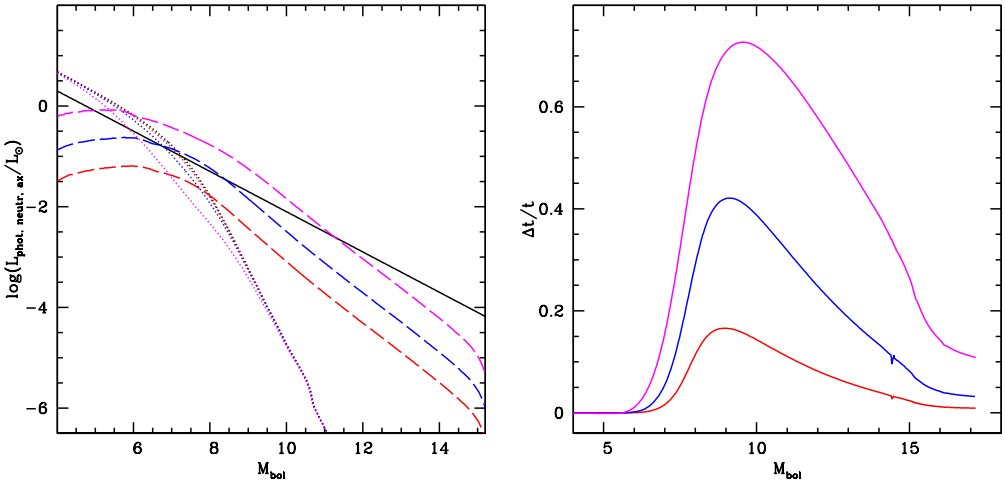

Figure 11: *Left* : Photon (solid line), plus neutrino (dotted lines) and axion (dashed lines) luminosities with increasing values of $m_{\rm a}\cos^2\beta$ (equal to 0, 4, 8 and 17.5 meV), as a function of the bolometric magnitude M_{bol}, for a $0.61M_{\odot}$ WD model. The black dotted line displays the neutrino luminosity when $m_{\rm a}\cos^2\beta$=0. Red, blue and purple lines correspond to the case of $m_{\rm a}\cos^2\beta$=4, 8 and 17.5 meV, respectively. For increasing $m_{\rm a}\cos^2\beta$ the axion luminosity increases at fixed M_{bol}, and the neutrino luminosity very slightly decreases. *Right* : Fractional difference in cooling times between the calculations without axions and models including these particles (for $m_{\rm a}\cos^2\beta$ equal to 4, 8 and 17.5 meV as in the left panel and with the same colour coding). At a given $\rm M_{bol}$ differences increase with increasing $m_{\rm a}\cos^2\beta$.